Anion-exchange Mediated Synthesis of Hollow 2D Layered Materials and Heterostructures: Mechanism and Room-Temperature Gas Sensing Properties

Rajeev Kumar Rai, [a,1] Naveen Goyal, [a,1] Deepak Sharma, [b] Ranit Ram, [a] Koushik Jagadish, [a] Navakanta Bhat, [b] and N. Ravishankar [a, *]

[a] Materials Research Centre, Indian Institute of Science, 560012, India

[b] Centre for Nanoscience and Engineering, Indian Institute of Science, Bangalore-560012, India

[*]Email: nravi@iisc.ac.in

[1]Authors contributed equally

Abstract

The designing of nanostructures with unique morphologies and enhanced functionalities is a cornerstone of modern materials science. Ion exchange reactions in inorganic crystals offer a versatile approach for precisely controlling the composition, morphology and properties of the materials through stepwise transformations. In this study, we report the anion exchange-mediated conversion of 2D layered material SnS_2 into $SnSe_2$, with SnS_2-$SnSe_2$ lateral heterostructures as intermediates. This transformation, driven by the disparate diffusion rates of S^{2-} and Se^{2-} ions, leads to the generation of hexagonal nanorings of $SnSe_2$ (inaccessible by direct synthetic routes) via the Kirkendall effect. By carefully balancing the diffusion kinetics through concentration control, we also successfully synthesized continuous $SnSe_2$ nanosheets. To elucidate the anion exchange mechanism, we conducted a comprehensive investigation using electron microscopy techniques, varying parameters such as time, precursor concentration, and reagents. Our findings revealed that the exchange process initiates at the edges of the template SnS_2 nanosheets and progresses inward. Cross-sectional atomic-resolution electron microscopy of the interfaces and layer stacking in the SnS_2-$SnSe_2$ heterostructure uncovered numerous defects, attributed to ion migration and lattice mismatch, which were not detectable in planar views. Furthermore, as-synthesized materials are explored for gas-sensing applications. Our anion-exchange-derived SnS_2-$SnSe_2$ heterostructure and $SnSe_2$ exhibited exceptional selectivity and sensitivity towards NO_2 gas (response > 700%) at room temperature comparable to state-of-art sensors, significantly outperforming the pristine SnS_2 material, which required elevated temperatures (150°C) for optimal response. This study

underscores the potential of anion exchange as a powerful tool for designing novel nanomaterials with tailored properties and applications, particularly in the realm of gas sensing.

Introduction

Over the past decade, post-synthetic modification of inorganic nanocrystals through ion-exchange reactions has emerged as a powerful tool for fabrication of novel materials with tailored properties.[1,2] In a typical ion-exchange reaction, cations/anions of template nanocrystal are replaced by new cations/anions with maintenance of original anion/cation sublattice. The feasibility of these reactions is influenced by various thermodynamic and kinetic parameters, including association/dissociation energies, solubility products, temperature, reactant concentration and ion diffusion rates.[3,4] While cation-exchange reactions can occur rapidly at low temperatures, anion-exchange reactions often require harsh conditions due to the large size and slower diffusion of anions.[5–8] Moreover, preserving the cation sublattice integrity during anion-exchange remains a challenge and hence has been less explored as compared to cation-exchange reactions. Materials like metal chalcogenides and perovskites are ideal for these reactions due to their crystal structure and bonding characteristics.[9,10] In contrast, exploring ion exchange in polar covalent compounds (less ionic character) presents a significant challenge due to the absence of discrete charged species.

Herein, we explore anion-exchange reactions in layered metal dichalcogenides (LMDs). These materials possess a distinct layered structure characterized by polar covalent bonding between metal atoms and chalcogens within each layer, while the individual layers are weakly held together by van der Waals forces.[11–13] This inherent anisotropy in bonding influences the properties of LMDs significantly, particularly their layer-dependent behavior.[14–16] Moreover, heterostructure engineering, encompassing both vertical and lateral heterostructures, offers a promising avenue for further tailoring the properties of LMDs.[17–20] Recent research have shown several instances of lateral heterostructures, where dissimilar materials are integrated within the same atomic plane. This approach has yielded materials with properties exceeding those of their individual counterparts, opening doors for applications in electronics,[21,22] optoelectronics,[23] sensing,[24] and energy storage.[25]

Despite the established use of ion-exchange for forming lateral hybrid nanostructures in ionic compounds,[5,7] a comprehensive mechanistic understanding of this process in LMDs remains elusive. The complexity of anion-exchange reactions in LMDs can be understood from the fact

that even a simple cation-exchange reaction from SnS_2 to MoS_2 requires high temperatures (~ 300 °C) and long reaction times.[26] This highlights the challenges associated with LMDs-based anion-exchange and underscores the need for further exploration. Additionally, the interface between the components in lateral heterostructure profoundly influences their overall properties.[27–29] Hence, exploring the interface of the post-synthetic exchange-mediated heterostructures is crucial for both understanding the reaction mechanism and establishing structure-property correlations.

For our study, SnS_2 was chosen as the template for the anion-exchange synthesis of $SnSe_2$ due to their shared structural characteristics. Both materials possess hexagonal crystal structures with similar layer stacking sequences and each layer is formed by polar covalent bonds (ionic character ~13%).[30,31] Additionally, SnS_2 and $SnSe_2$ have garnered significant interest for gas sensing applications.[32–34] However, the substantial lattice mismatch (~ 4.2%) along the c-axis between SnS_2 and $SnSe_2$ poses a significant challenge for forming in-plane lateral heterostructure with sharp interfaces.

In this study, we present a novel anion-exchange strategy for synthesizing layered materials and their lateral heterostructures. Employing SnS_2 as a template, the anion-exchange process with selenium ions resulted in the formation of unique hexagonal nanoring structured $SnSe_2$. Such nanostructures are unique to LMDs and maximize the exposure of active edge sites, offering potential advantages for surface and edge-site-dependent application such as gas sensing. Mechanistic investigations using microscopy studies revealed an edge-initiated anion-exchange process, leading to the formation of lateral heterostructures with $SnSe_2$ on the outer periphery and SnS_2 at the core. By carefully controlling reaction time and precursor ratios, various lateral heterostructures of $SnSe_2$-SnS_2 were successfully synthesized. Cross-section STEM analysis was performed to extract the interface structure and layer stacking sequence within these heterostructures. The formation of a diffuse interface with numerous line defects was attributed to the accommodation of lattice mismatch and strain induced during the anion-exchange process, in contrast to the defect-free pristine SnS_2. Further, we explored the synthesized materials for room temperature gas-sensing application. Anion-exchange-mediated $SnSe_2$ and lateral heterostructures exhibited remarkable sensitivity towards NO_2 gas with extraordinary response value of 720 % for $SnSe_2$ and a low detection limit of 0.1 ppm. Our anion-exchange strategy for synthesizing the unique morphology of $SnSe_2$ and lateral heterostructures, along with comprehensive understanding of reaction mechanism and interface structure, can be extended to other layered materials for targeted applications.

Results and Discussion

The anion-exchange reaction in layered materials was employed to convert SnS_2 into $SnSe_2$ using Schlenk line hot-injection method. Sulphur ions within the SnS_2 structure were substituted with selenium ions by introducing reduced Se precursor into a reaction mixture containing SnS_2 nanosheets dispersed in oleyl amine (OlAm) and 1-octadecene (ODE) at 170 °C under inert atmosphere. The reaction was optimized at 290 °C for 4 h. As illustrated in **Figure 1(a),** the anion-exchange reaction proceeded in a stepwise manner. Initially, a lateral heterostructure of SnS_2-$SnSe_2$ formed while preserving the template hexagonal nanosheet morphology. Subsequently, complete conversion to $SnSe_2$ resulted in the formation of unique morphology having Kirkendall void in a hexagonal nanosheet (designated as hexagonal nanoring). This morphology evolution during the anion-exchange process was elucidated using microscopy studies. **Figure 1(b-d)** shows the bright-field (BF) TEM micrograph of template hexagonal SnS_2 nanosheet, lateral heterostructure hexagonal SnS_2-$SnSe_2$ nanosheet, and final product hexagonal $SnSe_2$ nanoring, respectively.

Anion-exchange conversion of SnS_2 to $SnSe_2$

Synthesis of template SnS_2 nanosheets were achieved using hydrothermal method at 150 °C employing $SnCl_2$, thiourea as precursors in aqueous environment. The detailed characterization of synthesized SnS_2 nanosheets is presented in **Figure S1**. As-obtained hexagonal SnS_2 nanosheets were found to be phase-pure and single crystalline in nature (for detail refer **supplementary information**). These nanosheets served as a template to synthesize $SnSe_2$ via anion-exchange synthetic technique.

Given the typically high energy barrier associated with anionic framework rearrangement and the slower diffusion rate of anions compared to cations, anion-exchange reactions often require high temperatures.[35] To optimize the anion-exchange process, a temperature range of 200-290 °C was investigated. The powder XRD pattern of the product obtained at various temperatures is presented in **Figure S2**. A gradual decrease in SnS_2 related peaks and concomitant increase in $SnSe_2$ related peaks with rise in temperature indicated an enhanced degree of anion-exchange at higher temperature. The powder XRD pattern of SnS_2 matched with JCPDS card no. 230677 having lattice parameters a = b = 3.65 Å, and c = 5.89 Å, whereas peaks corresponding to $SnSe_2$ matched with JCPDS card no. 230602 having lattice parameters a = b = 3.81 Å, and c= 6.14 Å. The product obtained at 290 °C, shows predominant peaks corresponding to $SnSe_2$, suggest

a higher temperature of 290 °C is required to govern the anion-exchange reaction. The complete characterization of anion-exchange reaction (290 °C, 4 h) product is presented in **Figure 2**.

Powder XRD was performed to investigate the phase purity and crystallinity of the anion-exchange product as shown in **Figure 2(a)**. Powder XRD pattern of obtained anion-exchange product completely matches with $SnSe_2$ (JCPDS no. 230602) with space group $P\bar{3}m1$. The presence of intense peaks corresponding to $SnSe_2$ with absence of precursor peaks (SnS_2 and Se) indicates the complete conversion of SnS_2 to highly crystalline $SnSe_2$. The morphology and microstructure of synthesized $SnSe_2$ were investigated using TEM and STEM. Low-magnification BF-TEM micrograph (**Figure 2(b)**) reveals the transformation of hexagonal SnS_2 nanosheets into $SnSe_2$ hexagonal nanorings with etched central regions. Bright spots in selected area electron diffraction (SAED) pattern along the [001] zone axis depicts the single crystalline nature of the $SnSe_2$ (**Figure 2(c)**), which is further corroborated by the HRTEM image (**Figure 2(d)**). The exchange fraction and subsequent distribution of S, Se was investigated through STEM-EDS. The STEM-EDS elemental distribution map confirms the successful anion-exchange process, showing a negligible amount of S and a uniform distribution of Se and Sn throughout the hexagonal nanoring framework **(Figure 2(e))**. Further atomic structure of $SnSe_2$ was revealed using aberration-corrected HAADF-STEM imaging. Atomic resolution HAADF-STEM image (**Figure 2(f)**) reveals the 1T-phase of $SnSe_2$ along [001] with octahedral coordination of Se around Sn atoms. (inset shows the low-magnification image of corresponding $SnSe_2$).

The formation of hollow $SnSe_2$ nanosheet during anion-exchange can be attributed to the Kirkendall effect and surface reconstruction.[36,37] This phenomenon mainly arise due to the disparity in the ionic radii and corresponding diffusion coefficient of S^{2-} and Se^{2-} ions. The smaller S^{2-} ions (1.84 Å) exhibit a higher diffusion coefficient compared to Se^{2-} ions (1.98 Å).[38] Consequently, S^{2-} ions diffuse outwards at a faster rate than Se^{2-} ions diffuse inwards, leading to the generation of vacancies inside the nanosheet. These vacancies cluster together to form Kirkendall void, while maintaining the overall hexagonal framework by surface reconstruction with same orientation. After anion exchange reactions, an increase in the lateral dimension of $SnSe_2$ is observed compared to parent SnS_2. The width distribution plot of template SnS_2, final product $SnSe_2$, and void in $SnSe_2$ is shown in **Figure S3**. The average lateral dimension of $SnSe_2$ nanosheets is ~1.5 times that of SnS_2, suggesting that, in addition to anions, Sn^{4+} cations also diffuse from central region to the edge of nanosheet, bonding with incoming Se^{2-} to form $SnSe_2$.

The formation of the Kirkendall void largely depends on the difference in diffusion flux of the incoming and outgoing ions.[39] To mitigate this void formation, and obtain continuous hexagonal $SnSe_2$ nanosheets, the diffusion rates of both ions has to be balanced, which can be achieved by increasing the concentration of the slower diffusing ion. As shown in **Figure S4 (a-b)** employing a ten-fold excess of Se ions relative to SnS_2, resulted in the formation of solid hexagonal $SnSe_2$ nanosheets. The single crystalline nature of these nanosheets is confirmed by SAED pattern (**Figure S4(c)**) along [001] zone axis. Therefore, by adjusting the Se precursor concentration during the anion-exchange process, it is possible to tune the morphology of $SnSe_2$ while preserving the hexagonal framework and single crystalline nature of template SnS_2.

Time-dependent anion-exchange mechanism

To elucidate the mechanistic pathway, and morphology evolution during anion-exchange process, structural investigation of partial exchange products obtained at different time interval can provide valuable insights. A series of TEM micrographs and STEM-EDS maps were acquired typically for 5 mins, 30 mins, 1 h and 4 h products to illustrate the effect of time, as shown in **Figure 3**. Initially, the incoming Se^{2-} ion tends to percolate the SnS_2 nanosheets from the edges to initiate the exchange reaction resulting in edge deformation, as illustrated by the exchange product after 5 mins (**Figure 3(a)**). With the progress of exchange, edge reconstruction became apparent, as evident from BF-TEM micrograph of 30 mins product in **Figure 3(b)**. SAED patterns acquired from the edge (region-1) and centre (region-2) of the nanosheet (**Figure 3(c, d)**), reveals double spots in region-1, which are indexed to both SnS_2 and $SnSe_2$ phases along [001] zone axis, indicating the formation of a lateral heterostructure with epitaxial relation: $(100)_{SnS2}$ // $(100)_{SnSe2}$. In contrast, the SAED pattern from the region-2 corresponds to SnS_2 along [001] zone axis. This suggests anion-exchange process started from the edge of the nanosheet and leads to the formation of lateral heterostructure of SnS_2-$SnSe_2$ with same orientation and retention of original SnS_2 morphology. With the progress of the reaction, a contrast difference between the edge and centre implies the thinning of SnS_2 nanosheets in the centre due to the fast outward diffusion of S^{2-} and slow inward diffusion of Se^{2-} (1 h product, **Figure 3(e)**), ultimately leading to the hexagonal nanoring formation. After 4 h of exchange reaction, a solid nanostructure of $SnSe_2$ with sharp edges and a hole in the centre **(Figure 3(f))** is observed.

HAADF-STEM images and corresponding STEM-EDS mapping further corroborated the morphology evolution and elemental distribution during the exchange process as shown in **Figure 3(g)**. The EDS maps align with the TEM observation, showing the higher concentration of Se on the edges in the early stage of the reaction, indicative of Se^{2-} ions percolation from the edges. A lateral heterostructure of SnS_2-$SnSe_2$ can be clearly seen in 30 mins product with SnS_2 rich centre and $SnSe_2$ rich edges. Over time with increase in the amount of $SnSe_2$, the formation of lower contrast region in the centre of the HAADF-STEM image (Inset: **Figure 3(g)**) confirms the thinning of the nanosheet and consequently, the formation of Kirkendall void.

To understand the initiation of the exchange process at the edge of the nanosheet, an atomic model of a layered SnS_2 structure along [100] zone axis is presented (**Figure 3(h)**), highlighting the potential attacking sites for incoming Se^{2-} ions. The propensity of Se^{2-} ions to donate electrons to vacant d-orbitals of Sn atoms can facilitate the formation of dative bonds, while simultaneously triggering the breakage of Sn-S bonds. Moreover, the van der Waal gap within the SnS_2 layers provide a facile pathway for Se^{2-} ion migration into the interior of the nanosheet. However, steric effects arising from extensive lone-pair repulsion between sulphur and selenium ions presumably hinder the attack of Se^{2-} ions from the top/bottom surfaces of the SnS_2. This explains the initiation of the anion-exchange reaction at the edges of the nanosheet.

Further, to understand the effect of the various reagents used in anion-exchange reaction, control experiments were conducted. To investigate the impact of OlAm and ODE without adding the Se precursor on the exchange reaction, SnS_2 was just heated in OlAm and ODE at 290 °C for 2 h. Characterization of the product (**Figure S5)** reveals no change in PXRD pattern, nanosheet morphology and SAED pattern compared to template SnS_2, suggests that these reaction conditions did not alter the structure and morphology of SnS_2. Similarly in the same reaction conditions the effect of 1-DDT on the morphology of SnS_2 was investigated by adding the 1-DDT equivalent to the Se-precursor in the reaction. Powder XRD pattern reveals that heating SnS_2 in the OlAm, ODE, and 1-DDT does not have any structural impact on SnS_2 crystallinity **(Figure S6)**. However, the morphology of SnS_2 undergoes a slight deformation (**Figure S6(b)**). The SAED analysis (**Figure S6(c)**) shows that SnS_2 is still present as single crystalline 2D sheets. These control experiments reveal that the used reagents do not affect the structure and morphology of template SnS_2 until Se precursor is added.

The role of ODE in the anion-exchange was examined by performing the reaction without ODE. Powder XRD analysis of the product reveals the incomplete conversion to $SnSe_2$ with

persistent SnS_2 peaks even after 2 h (**Figure S7(a)**). The TEM micrograph shown in **Figure S7(b)** reveals that $SnSe_2$-SnS_2 sheet has slightly lost its structural integrity but shows the thinning in the centre. The SAED pattern from the centre and edge of the sheet also aligns with the partial exchange. The SAED pattern from the edge corresponds to $SnSe_2$, whereas the centre of the nanosheets matches that of SnS_2 (**Figure S7 (c-d)**). These findings highlight the crucial role of ODE in maintaining the overall morphology and facilitating the fast completion of exchange reaction. From control experiments, it can be concluded that the formation of hollow hexagonal $SnSe_2$ nanosheets is not attributable to the solvents (OlAm, 1-DDT or ODE) but rather rises from the Kirkendall effect. Additionally, the lattice mismatch and the associated stress induced by volume changes at the interface may contribute to the etching of the core regions.

Lateral heterostructure formation by varying precursor ratio

The mechanistic study has shown that the anion-exchange reactions are sluggish and require high temperature (290 °C) and a longer time (4 h) for completion. Hence, taking advantage of the sluggish kinetics of anion-exchange and the fact that exchange initiates from the edges and moves inward through the diffusion of ions, we extended our reaction scheme to synthesize lateral heterostructures. The lateral heterostructures can be synthesized in two ways: (1) Controlling the time of the exchange reaction (as shown in the time-dependent reaction mechanism) and (2) Controlling the amount of Se-precursor injected. Herein, the lateral heterostructures of $SnSe_2$-SnS_2 were synthesized by varying amounts of reduced Se precursor as mentioned in **Table 1**. **Figure 4(a)** shows the powder XRD pattern of ion exchange products with addition of 0.5 ml, 1 ml, 1.5 ml, and 2 ml of reduced Se precursor, corresponding to the theoretical replacement of 25%, 50%, 75% and 100% of the S in SnS_2. The powder XRD pattern reveals an increase in the peak intensity of $SnSe_2$ with an increasing fraction of Se^{2-} ions in the reaction. Upon addition of 2 ml Se-precursor, predominantly $SnSe_2$ peaks are observed.

Microstructural characterization of the partial exchange product with 1 ml of reduced Se precursor is shown in **Figure 4(b-f)**. The BF TEM image in **Figure 4(b)** depicts a sharp-edged hexagonal nanostructure with a contrast difference between the centre and edge of the nanosheet. SAED patterns from regions marked as 1 and 2 (**Figure 4(c-d))** show single-crystalline patterns corresponding to $SnSe_2$ and SnS_2 along [001] zone axis, respectively. **Figure 4(e)** demonstrates the SAED pattern from the interface (shown in the inset), exhibiting

double spots revealing the formation of epitaxial heterostructure based on $SnSe_2$-SnS_2. The HAADF-STEM image and corresponding elemental distribution maps in **Figure 4(f)** further corroborate the TEM analysis, with $SnSe_2$ located at the edges and SnS_2 at the centre.
Similarly, microstructural features of the partial exchange with 0.5 ml and 1.5 ml of Se-precursors are shown in **Figure S8,** and **S9** respectively (for details refer **supporting information**).
All the partially exchanged products exhibit a uniform distribution of Sn, with $SnSe_2$ at the edges and SnS_2 forming the nanostructure core. The extent of anion-exchange and etching at the central region is observed to increase with the addition of larger amount of Se precursor as evident from **Figure S8, 4** and **S9**.

Structure of interface and defect analysis

The control experiments convincingly demonstrate the initiation of the anion-exchange transformation at the edges, propagating inwards to form a lateral heterostructure of $SnSe_2$-SnS_2. However, several key questions remain unaddressed - (1) Depth of exchange: Layers in SnS_2 are joined together by van der Waals gap and provide pathway for facile migration of ions. So, it is crucial to determine whether this exchange is confined to few topmost layers or if it occurs simultaneously throughout the entire SnS_2 structure. (2) Structure of interface: To elucidate whether the interface is atomically sharp or diffuse with intermixing of SnS_2 and $SnSe_2$. (3) Lattice mismatch accommodation: SnS_2 and $SnSe_2$ possess a significant lattice mismatch ~4.2% along the c-axis in which the layers are stacked. So, it is important to understand how this lattice mismatch is compensated at the interface to achieve structural stability. (4) Defect Formation: The ion-exchange process might induce the defects within the newly formed heterostructure. A thorough characterization is essential to identify the types of defects generated during this transformation.

In order to comprehensively address the aforementioned questions, it is imperative to investigate the layer stacking sequence of the interface, which can be achieved by direct imaging of the side view of nanosheet perpendicular to [001]. For this, cross-sectional HAADF-STEM imaging was performed. A schematic for FIB lamella preparation for the cross-section analysis of the nanosheet is shown in **Figure S10(a)**. Lateral heterostructure nanosheet was milled parallel to the [001] direction to enable direct visualization of the side view containing two interfaces under the electron beam. **Figure S10 (b and c)** shows the SEM

micrographs of the nanosheet used for the lamella preparation and the prepared TEM lamella. The HAADF-STEM image of the TEM lamella shows the side view of SnS_2-$SnSe_2$ heterostructure sandwiched between Pt and Si **(Figure S10 (d))**. A relative high-resolution HAADF-STEM image (**Figure S11)** displays non-uniform contrast between the edge and the centre, indicative of a lateral heterostructure with two distinct interfaces. The Z-contrast mechanism[40] of HAADF-STEM imaging attributed this contrast variation to compositional differences. The experimental observation of the etching of the core region is also clearly visible with pits forming in the centre of the nanosheet. The STEM-EDS map of the entire sheet further confirms the presence of two interfaces with Sn being uniformly distributed, while S and Se are segregated at the core and edge of the lamella, respectively (**Figure S11**).

STEM-EDS mapping of a representative SnS_2-$SnSe_2$ interface (**Figure 5(a))** reveals a small overlap between S and Se signals, suggesting a diffuse interface has formed with intermixing of SnS_2 and $SnSe_2$. The EDS maps further confirm that the anion-exchange process occurs across all the layers on the edges rather being confined to the top surface. Three distinct regions are identified near the heterostructure interface (**Figure 5(b)**): $SnSe_2$ (region-1), the mixed interface (region-2), and SnS_2 (region-3). High resolution HAADF-STEM images from region-1 and region-3 are shown in **Figure 5(c-d),** clearly depicting the 1T phase of $SnSe_2$ and SnS_2, respectively, indicating a topotactic exchange reaction. Lattice parameter measurement of $SnSe_2$ reveals a (001) interlayer spacing of 6.4 Å. The observed expansion of the c-axis parameter compared to the ideal spacing (6.14 Å) can be attributed to the ion migration and associated layer expansion during the exchange reaction.

High-resolution HAADF-STEM imaging of the interface (region-2) (**Figure 5(e)**) reveals a mixed phase of SnS_2-$SnSe_2$ as double spots correspond to $(1\bar{1}0)$ plane observed in the FFT (shown in inset) along [110] zone axis. A reduced (001) spacing of ~6.2 Å relative to the pure $SnSe_2$ phase (6.4 Å) was observed, further supporting the mixed-phase nature of the interface. Careful examination of the HAADF-STEM images of the interface at different magnification (**Figure 5(e)** and **6(a)**) shows additional interlayer gap, exceeding their typical van der Waals gap, originating from the interface and extending into the $SnSe_2$ region. These gaps are identified as line defects particularly edge dislocations, characterized by the presence of extra half layer (as marked) towards the SnS_2 side. These line defects appear to compensate for the strain induced due to lattice mismatch of ~4.2% along the c-axis between SnS_2 and $SnSe_2$. Considering the theoretical c-axis lattice parameter of SnS_2 (5.89 Å) and $SnSe_2$ (6.14 Å), the

expected spacing between the edge dislocations is approximately 14 nm. Measurements of the observed gap spacing within the interface region (**Figure S12)** yielded an average value of 12.6 nm (closer to the theoretical value) with a range of 7.5 – 20.1 nm. This randomness in the line defects can be attributed to the variability in interlayer spacing along (001) in $SnSe_2$ and interface regions due to ion migration channels.

An atomic-resolution HAADF-STEM image of the edge dislocation is presented in **Figure 6(b)** (inset: Burgers circuit). The burger vector $\mathbf{b}_R$ is measured around the burger circuit ABCDEA and found to be $\mathbf{b}_R$ = [001]. The presence of line defects and migration of ions also induces bending of the layers near the interface, resulting in a warped and disordered structure (**Figure 6(c)**). Additionally, intercalated species are observed (as highlighted in **Figure 6(d)**) between the SnS_2 layers, further confirming the migration of ions occur in the van der Waals gap of the layered material. **Figure S13** provides an overview of the interface, highlighting numerous defects marked by circles/ellipses, further confirming the presence of defected interface during the anion-exchange process. An atomic model illustrating the interface structure with defects and ion migration within the interlayer space is depicted in **Figure 6(e)**.

To confirm that the observed defects originated solely from the anion-exchange process, a pristine SnS_2 sample was subjected to cross-section analysis. HAADF-SETM micrograph in **Figure S14(a)** shows the side view of the TEM lamella of prepared SnS_2 sample using FIB cross-section. Corresponding high-resolution image (**Figure S14(b)**) reveals continuous SnS_2 layers devoid of any defects. An atomic resolution image of the corresponding region (**Figure S14(c)**) shows the standard 1T phase arrangement of SnS_2. The absence of defects in pristine SnS_2 sample provides conclusive evidence that the defects observed in the anion-exchange product are indeed induced by the exchange process.

Gas-sensing measurement

Pristine SnS_2 and $SnSe_2$ have demonstrated their potential application as gas sensors selectively for NO_2 gas detection.[32,41] Ruozhen et al., investigated a $SnSe_2$-SnS_2 van der Waals heterostructure revealing an enhanced NO_2 sensing response at room temperature.[34] This improvement is attributed to the formation of an interface and the resulting charge transfer between SnS_2 and $SnSe_2$. However, NO_2 gas sensing performance of anion-exchange derived $SnSe_2$ hexagonal nanorings and their lateral heterostructure remain unexplored.

Herein, we have tested template SnS_2 nanosheets, 1:1 lateral heterostructure of $SnSe_2$-SnS_2 and $SnSe_2$ hexagonal nanorings for NO_2 gas sensing performance. **Figure 7(a)** represents the concentration-dependent current-time behaviour of all three samples where the concentration of target gas (NO_2) varied from 0.1 ppm to 5 ppm. Pristine SnS_2 showed very high resistance and resulted in poor gas sensing performance at room temperature. Hence, all gas sensing properties of SnS_2 were optimized at 150 °C, while both $SnSe_2$ and lateral heterostructure demonstrated remarkable performance even at room temperature. On exposure to electrophilic NO_2 gas, all samples exhibited a decrease in current values, indicative of n-type behaviour where electrons transfer from the sample to the NO_2 gas. Schematic depicting transfer of electron from the SnS_2-$SnSe_2$ surface to NO_2 gas is depicted in **Figure 7(b)**. Prior to NO_2 gas purging (at t = 0 min), the initial current levels (y-axis) of the samples follows the order: SnS_2 (20-30 nA) < SnS_2-$SnSe_2$ (400-500 nA) < $SnSe_2$ (~ 1200 nA). This observed current levels directly relates with the electron concentration in the sample, signifies an increase in electron concentration from SnS_2 to $SnSe_2$. Further, we have calculated response (%) by using the following equation.[42]

$Response\ (\%) = [(I_{air} - I_{gas}) / I_{gas}] \times 100$ for oxidizing gas

$Response\ (\%) = [(I_{gas} - I_{air}) / I_{air}] \times 100$ for reducing gas

Where I_{air} is the sensor current during exposure to dry air and I_{gas} is the sensor current during exposure to target gas.

Figure 7(c) represents the response (%) of SnS_2-$SnSe_2$ heterostructure and $SnSe_2$ hexagonal nanorings to varying NO_2 gas concentrations at room temperature. A direct corelation between the NO_2 gas concentration and response (%) is observed for both materials. An extraordinary response value of around 720 % is achieved at 2 ppm NO_2 gas for $SnSe_2$, which is remarkably higher than previous reports.[32,34,43–45] This enhancement is attributed to the anion-exchange mediated hollowness in the $SnSe_2$ nanosheet, which possess a larger lateral dimension with void offering more active sites for NO_2 adsorption and interaction compared to the SnS_2-$SnSe_2$ heterostructure. The response (%) curve with varying concentration of NO_2 at 150 °C for pristine SnS_2 is shown in **Figure S15**.

Next, we have demonstrated the repeatability test of our sensors at 2 ppm NO_2 gas by subjecting them to multiple cycles as shown in **Figure 7(d)**. Both SnS_2 and $SnSe_2$ exhibits minor degradation in the current levels over repeated exposure of NO_2 gas where full recovery to

baseline current was missing, might be due to surface poisoning. However, repeatability test of SnS_2-$SnSe_2$ heterostructure shows consistent performance of the sensor, suggests fast charge transfer at n-n lateral heterojunction interface reducing the surface poisoning. This behaviour is likely attributed to the internal transfer of electrons from $SnSe_2$ to SnS_2, facilitated by the lower Fermi level of SnS_2 (5.1 eV) compared to $SnSe_2$ (4.9 eV).[34] Similar, fast charge transfer at the interface has been observed in case of vertical heterostructure of $SnSe_2$-SnS_2.[34]

Next, to access the selectivity of our sensors, a selectivity test was performed in the presence of various oxidizing and reducing gases (methane, ethylene, ethyl alcohol, SO_2, NH_3, NO_2, H_2, H_2S, CO and acetone). All three sensors exhibit exceptional selectivity towards NO_2 gas, with minute responses to other gases tested (**Figure 8).** A comparison of the sensing performance of all three variants is shown in **Table 2**, with a broader comparison with previously reported SnS_2 and $SnSe_2$-based sensors is provided in **Table S1**.

Overall, the anion-exchange synthesized $SnSe_2$-SnS_2 heterostructure and $SnSe_2$ demonstrated excellent gas sensing performance at room temperature, characterized by high response, selectivity, and repeatability. These findings highlight the potential of our synthesized materials for practical gas sensing applications.

Table 2 Summary of all the sensor operating parameters and performance.

Variant	**Operating Conditions**	**Current levels (nA)**	**Repeatability**	**Lowest limit of detection (ppm)**
SnS_2	150 °C	~20	Moderate	0.1
$SnSe_2$	RT	~1200	Moderate	0.2
$SnSe_2$- SnS_2	RT	~400	High	0.1

Conclusion

In this study, we have designed an anion-exchange-mediated synthesis of layered material $SnSe_2$ and their heterostructures $SnSe_2$-SnS_2. The anion-exchange transformation mechanism is exhibited using microscopy studies and found that exchange started from the edge of the template nanosheet and proceeded inwards leading to formation of Kirkendall void and

resultant hexagonal nanoring morphology of the final product $SnSe_2$. This designed strategy is further used to synthesize composition and time-dependent heterostructures. To gain insights into the interface and layer-sequence of the heterostructure, cross-section STEM imaging was performed. In a typical 1:1 composition heterostructure, the interface was found to be diffused with numerous defects at the bulk of the heterostructure mainly due to ion migration and to compensate for lattice mismatch between the c-axis of SnS_2 and $SnSe_2$. Further, these materials were explored for the gas sensing applications. Our synthesized materials $SnSe_2$-SnS_2 heterostructure and $SnSe_2$ demonstrated excellent selectivity towards NO_2 sensing at room temperature with the remarkable low limit of detection of 0.1 ppm. Notably, $SnSe_2$ exhibits a significant response value of 720 % highlighting the enhanced properties achieved through the anion-exchange synthesis method. Overall, this study presents the applicability of anion-exchange synthesis to design novel nano-heterostructures of layered materials and their transformation pathway, with in-depth analysis of the interface and development of room-temperature gas sensors.

Materials and Methods

Chemicals: All chemicals are used as obtained without any further purification. The chemicals used are $SnCl_2.2H_2O$ (97%, powder, Ranbaxy), thiourea (99%, powder, SDFCL), conc. HCl (34.5%, liquid, SDFCL), Se (99.9%, powder, Sigma Aldrich), Oleyl amine (OlAm, 50%, liquid, TCI), 1-dodecanethiol (1-DDT, 99%, liquid, Sigma Aldrich), 1-octadecene (ODE, 95%, Alfa Aesar), ethanol (EtOH, 99.9%, liquid, analytical CS reagent) and hexane (99%, liquid, SDFCL).

Synthesis of template SnS_2: The synthesis of SnS_2 has been carried out by a slightly modified hydrothermal method.[46] In a typical synthesis, 0.5 ml of conc. HCl was added to 10 ml of deionized water to make a homogeneous solution. Next, 1 mmol of $SnCl_2.2H_2O$ was added to it and the solution mixture was stirred for 30 min. Then, 8 mmol of thiourea was added to the solution and volume was made to 30 ml by adding deionized water. The whole mixture was stirred for the next 30 min and then transferred to a 50 ml Teflon-lined autoclave and kept at 150 °C for 48 h. After the reaction, the autoclave was cooled down to room temperature naturally. The product was washed with water several times and finally with ethanol. The product was dried at 60 °C for 1 h and used for further characterization and anion-exchange reactions.

Anion-exchange-mediated synthesis of $SnSe_2$

Reduced Se precursor solution: Firstly, the reduced Se-precursor was synthesized, which is used as a guest anion precursor in the anion-exchange reaction. In a round bottom flask, 1 mmol of Se powder is dissolved in a 1:1 volume ratio of OlAm and 1-DDT with a total volume of 10 ml. The mixture was degassed under vacuum at 80 ℃ and was kept for 1 h under argon atmosphere for the complete reduction of Se powder.

Anion-exchange synthesis: In a typical anion-exchange reaction, 0.1 mmol of as-synthesized SnS_2 was taken into a 50 ml round-bottom flask, 5 ml OlAm and 2 ml ODE were added to it. The whole mixture was then degassed under vacuum with stirring at 120 ℃ for 15 min. The flask was then filled with argon gas, and the temperature raised to 170 °C and was kept for the next 10 min. The required amount of reduced Se precursor was rapidly injected into the flask, and the temperature of the flask was raised to 290 °C. The solution mixture was then stirred for another 4 h for the complete conversion of SnS_2 to $SnSe_2$.

The heterostructure of SnS_2-$SnSe_2$ has been synthesized by partial exchange reaction with varying precursor ratio, and time of the reaction. The reaction conditions employed for the synthesis of various heterostructures are mentioned in **Table 1**.

Table 1. Reaction conditions to perform anion-exchange with different fractions of exchange.

Sample Name	**Amount of Se-Precursor**	**Reaction condition (T, t)**
$SnSe_2$	2 ml	290 ℃, 4 h
$(SnSe_2)_{0.75}$-$(SnS_2)_{0.25}$	1.5 ml	290 ℃, 2 h
$(SnSe_2)_{0.5}$-$(SnS_2)_{0.5}$	1 ml	290 ℃, 2 h
$(SnSe_2)_{0.25}$-$(SnS_2)_{0.75}$	0.5 ml	290 ℃, 2 h

Characterization: As-synthesized nanostructures were characterized using different techniques. Phase purity and crystal structure of as-synthesized materials were studied using a powder X-ray diffraction (PXRD) pattern collected over the range of 10 ° to 60 ° using PANalytical X'pert Pro equipped with Cu K_α (λ =1.5418 Å). The morphology and microstructural characterization were performed using scanning electron microscope (SEM) and transmission electron microscope (TEM). SEM was performed using Ultra-55, Zeiss field-emission equipped with EDS. TEM was performed using the FEI Tecnai T20 ST microscope, operating at 200 kV. High-angle annular dark-field (HAADF) scanning transmission electron

microscope (STEM) imaging and energy dispersive X-ray spectroscopy (EDS) were performed using an aberration-corrected FEI Titan G2 (80-300) operating at 300 kV. For TEM and STEM imaging, samples were prepared by dispersing the as-synthesized materials in an ethanol-hexane mixture and drop-cast on a carbon-coated Cu grid. For cross-sectional STEM analysis, TEM lamella has been prepared by employing a focused ion-beam technique in an FEI Scios dual beam instrument, in which a 5 kV electron beam is utilized for Pt deposition as a protective layer and a 30 kV ion beam for further milling.

Chemiresistive sensor development and characterization: Inter-digited electrodes (IDE) were patterned using a standard CMOS fabrication route.[47] 100 µL of the as-synthesized products SnS_2, $SnSe_2$-SnS_2 hybrid and $SnSe_2$ were drop-cast onto the fabricated IDE, followed by substrate heating at 80 °C for 1 h. All gas sensing measurements for $SnSe_2$-SnS_2 were optimized at 5 V with a Keithley 2450 source meter at room temperature. As-fabricated $SnSe_2$-SnS_2 sensor was placed in the customized sensing chamber where an appropriate proportion of dry air (80% N_2 and 20% O_2) and target gas (NO_2) was mixed to expose a specific concentration to the sensor via the Alicat Mass flow controller. The ON and OFF time of gas exposure was programmed to be 15 minutes.

Acknowledgement

RKR, NG and NR acknowledge the Advanced Facilities for Microscopy and Microanalysis (AFMM), IISc for providing the electron microscopy facilities. NG thanks Prime Minister Research Fellowship. NR acknowledges research grant from SERB (CRG/2023/003481) and Nano Mission, DST for financial support.

Notes

The authors declare no competing financial interest.

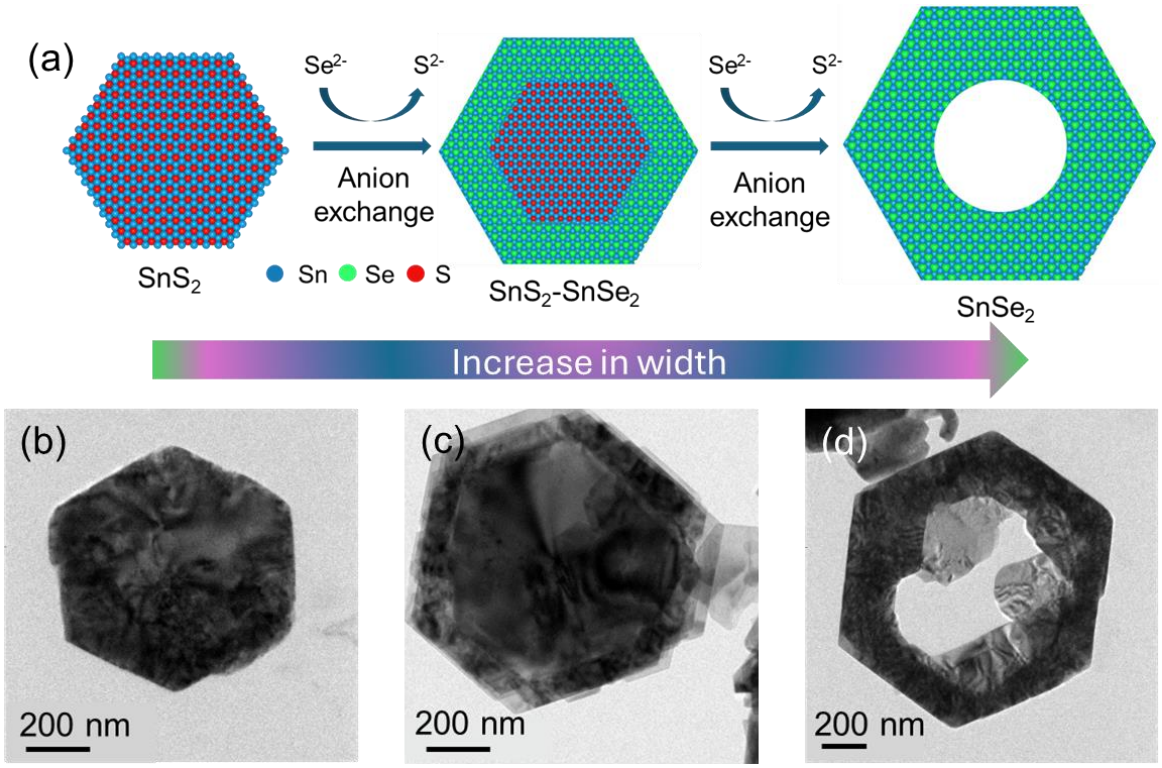

Figure 1: (a) Schematic demonstrating the morphology evolution during anion-exchange reaction. Hexagonal nanosheet of template SnS_2 is converted into hollow hexagonal nanosheet of $SnSe_2$ with increase in lateral dimension; **(b-d)** Low-magnification TEM micrographs of template SnS_2, intermediate lateral heterostructure of SnS_2-$SnSe_2$ and final product $SnSe_2$, respectively.

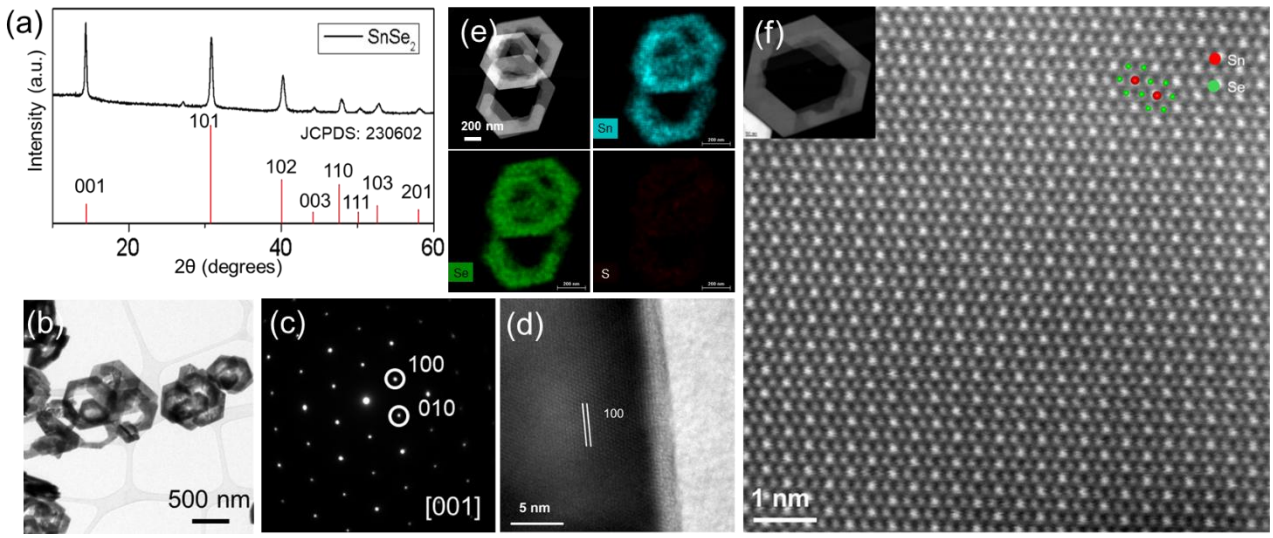

Figure 2: Characterization of anion-exchange product $SnSe_2$; **(a)** PXRD pattern; **(b)** low-magnification TEM micrograph; **(c)** SAED pattern along [001] zone axis; **(d)** HRTEM micrograph resolving (100) lattice plane; **(e)** HAADF-STEM micrograph and elemental distribution maps of Sn, Se and S, respectively and **(f)** Atomic resolution HAADF-STEM image showing the 1T phase arrangement of Sn and Se (inset: corresponding low magnification image).

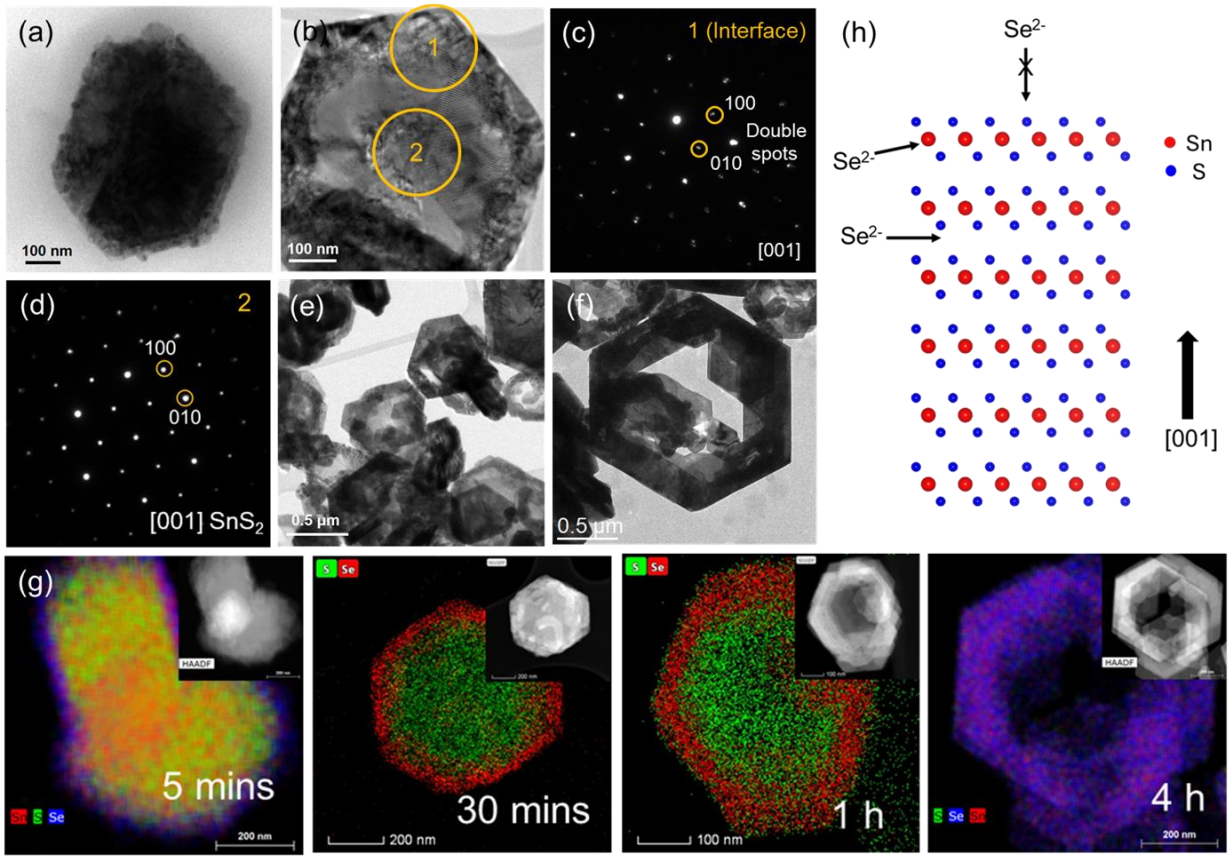

Figure 3: Time-dependent anion-exchange reaction mechanism. **(a-b)** Low-magnification TEM micrographs after 5 and 30 mins of the reaction, respectively; **(c-d)** SAED pattern from region 1 and 2 marked in (b); **(e-f)** Low-magnification BF TEM micrographs after 1 and 4 h of the reaction, respectively; **(g)** STEM-EDS map after 5 mins, 30 mins, 1 h and 4 h respectively and **(h)** Schematic showing possible attacking sites for incoming Se^{2-} ions to initiate the anion-exchange reaction.

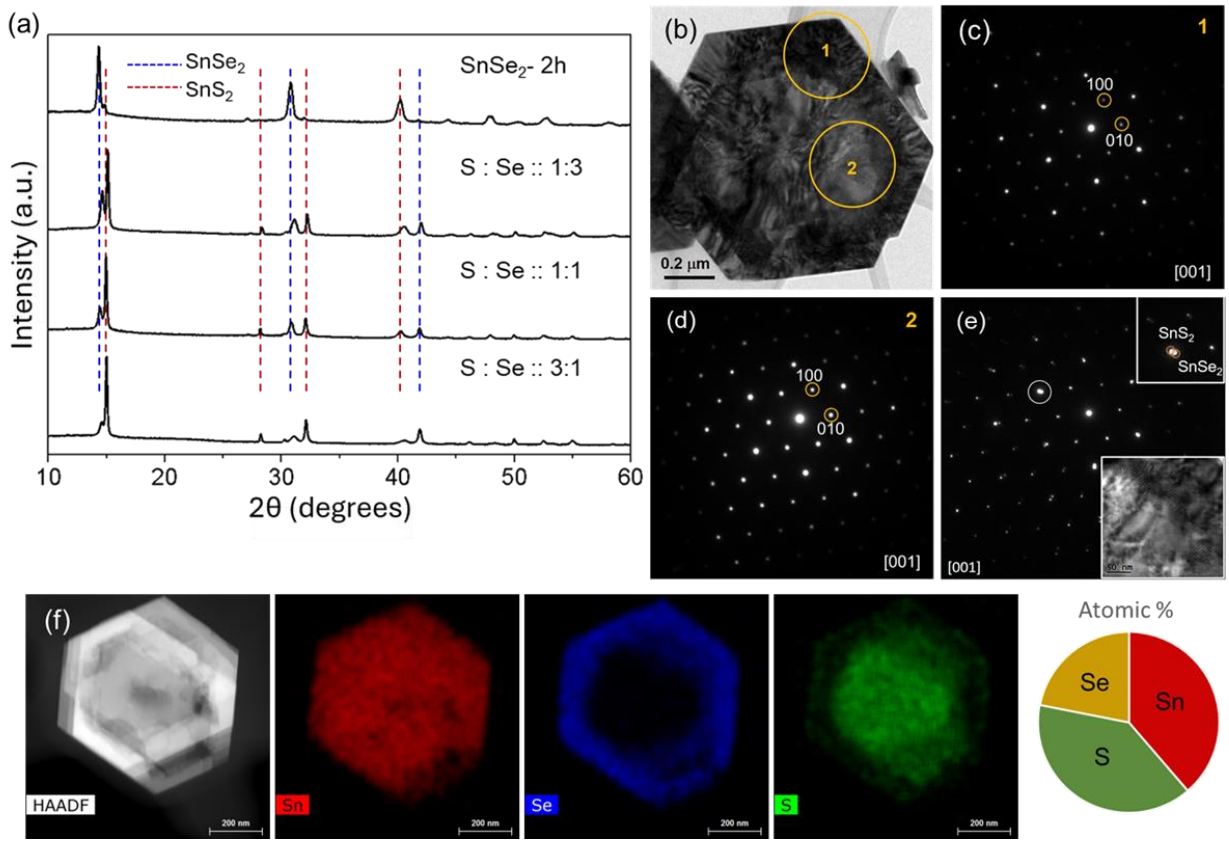

Figure 4: Anion-exchange mediated synthesis of lateral heterostructures; **(a)** Powder XRD patterns of the product obtained with different ratios of Se-precursor added. Microstructural characterization of the product obtained upon addition of 1 ml Se-precursor: **(b)** TEM micrograph; **(c-d)** SAED pattern from regions 1 and 2 marked in (b), respectively; **(e)** SAED pattern from the interface showing double spots (insets: top- zoomed-in pattern, bottom- the interface area) and **(f)** HAADF-STEM and element distribution maps depicting formation of 1:1 lateral heterostructure.

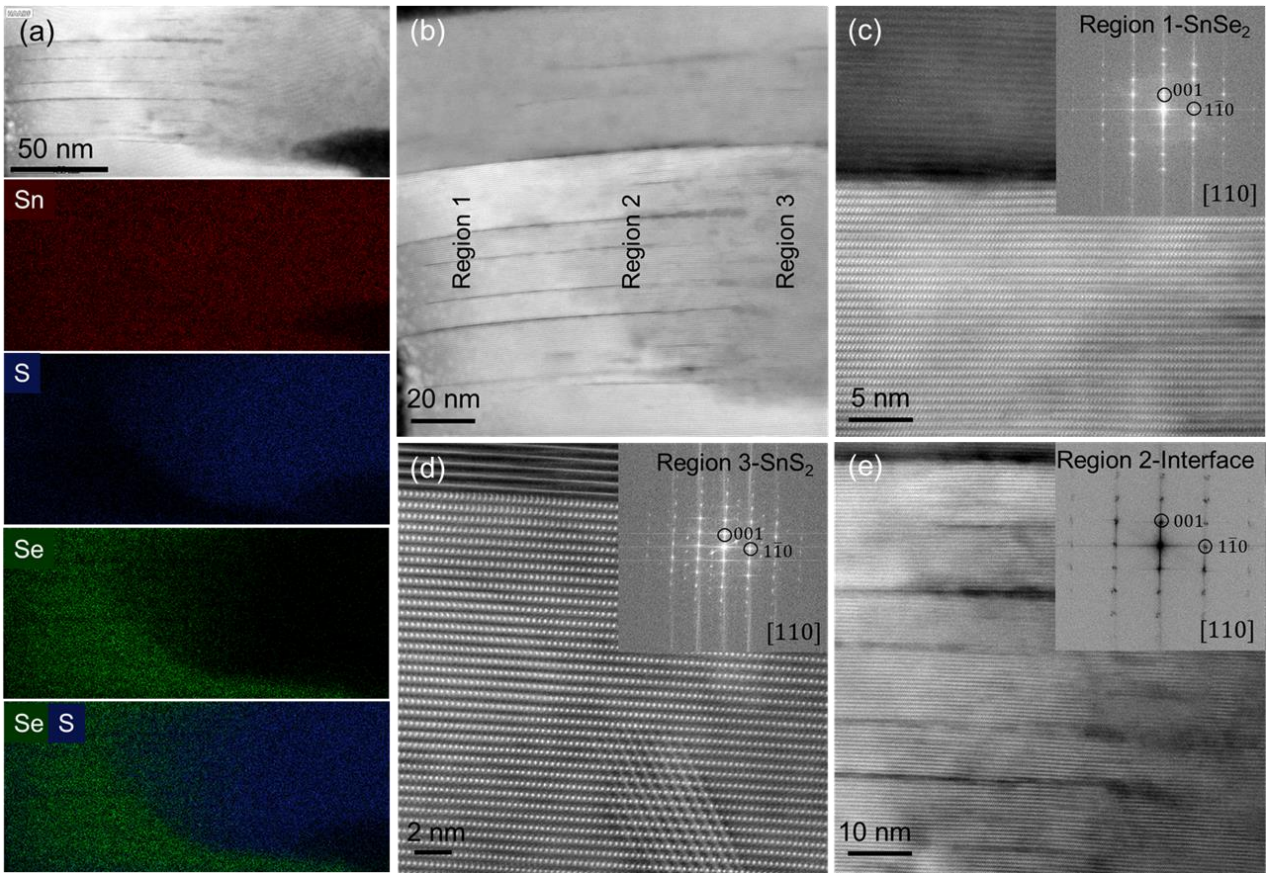

Figure 5: Cross-section STEM analysis of the 1:1 SnS_2-$SnSe_2$ heterostructure; **(a)** STEM-EDS map of side view of nanosheet depicting elemental distribution of Sn, S, and Se, respectively; **(b)** HAADF-STEM micrograph of side view showing three regions corresponding to $SnSe_2$, interface and SnS_2; **(c-d)** Atomic resolution images of region-1 and 3 belongs to $SnSe_2$ and SnS_2 respectively, showing 1T phase arrangement and **(e)** HAADF-STEM image of the region-2 interface (Inset: FFT of the respective regions).

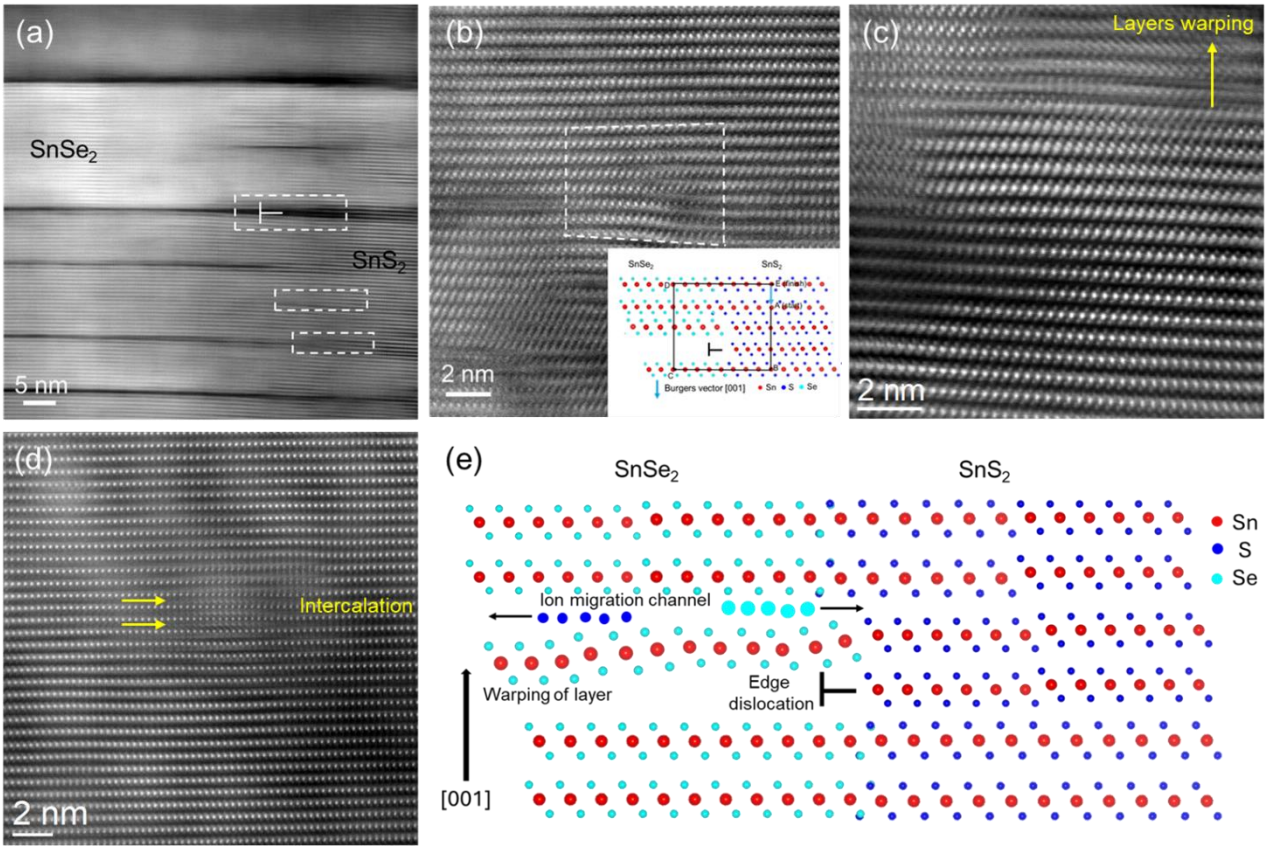

Figure 6: Defect analysis of the interface region in the heterostructure; **(a)** HAADF-STEM micrograph of the enlarged view of the interface showing multiple line defects originating from SnS_2 and propagated in the $SnSe_2$ region; **(b)** High resolution STEM image of the interface showing line dislocations (Inset: Burgers circuit); **(c)** Atomic resolution image showing disordered structure and warping of layers during anion-exchange; **(d)** Atomic resolution image from SnS_2 region showing ion migration through the nano-channels between the layers; **(e)** Schematic illustrating the interface structure and presence of numerous defects through atomic models during anion-exchange process.

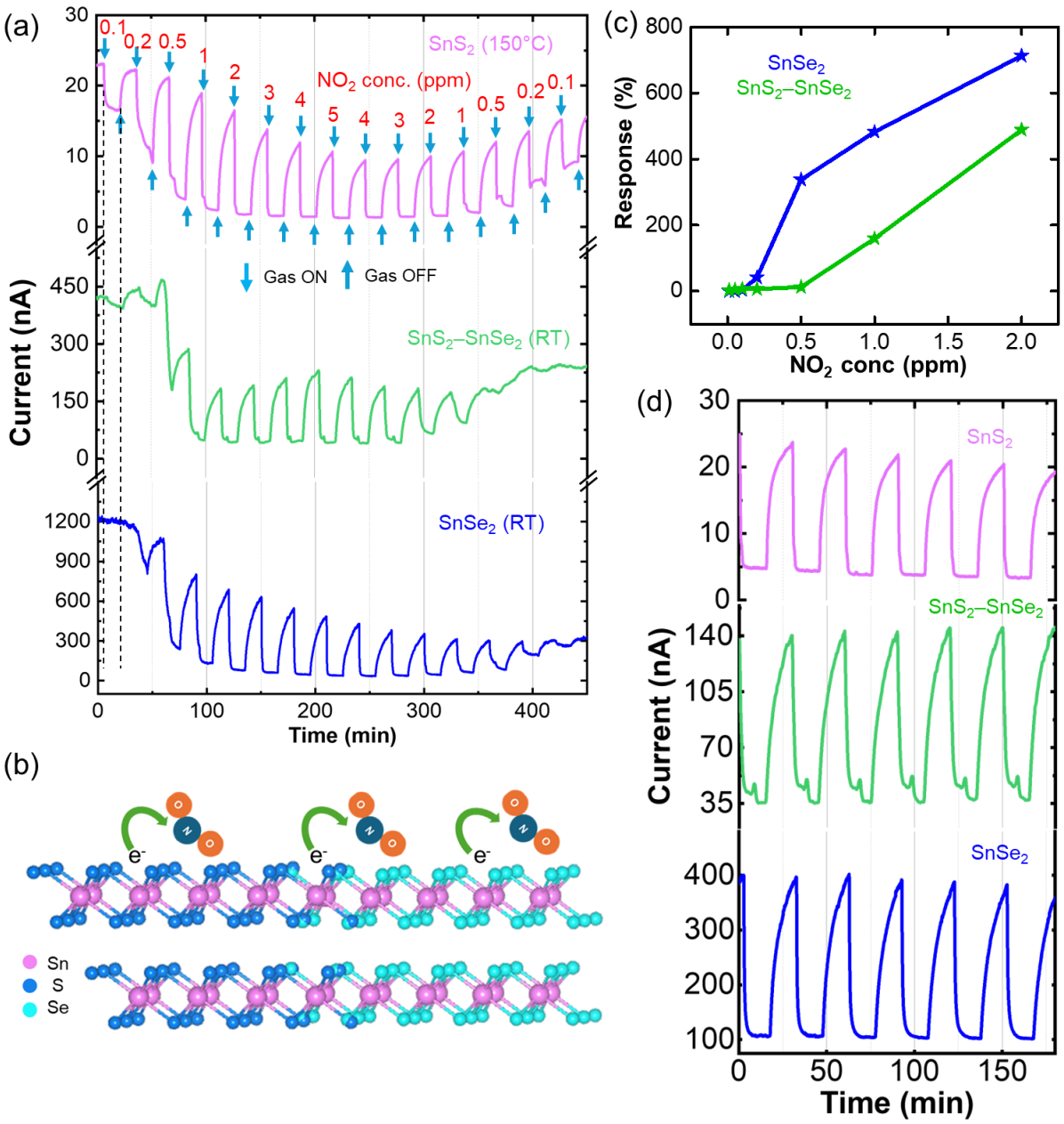

Figure 7: Gas sensing performance of synthesized samples- pristine SnS_2 (150°C), $SnSe_2$-SnS_2 heterostructure (RT) and $SnSe_2$ (RT); **(a)** I-t curve of the sensors with varying concentration of NO_2; **(b)** Schematic depicting transfer of electrons from the n-type $SnS_2/SnSe_2$ to NO_2 gas molecules; **(c)** Response (%) of the sensors with varying NO_2 concentration; **(d)** Repeatability curve of the sensors at 2 ppm NO_2 concentration.

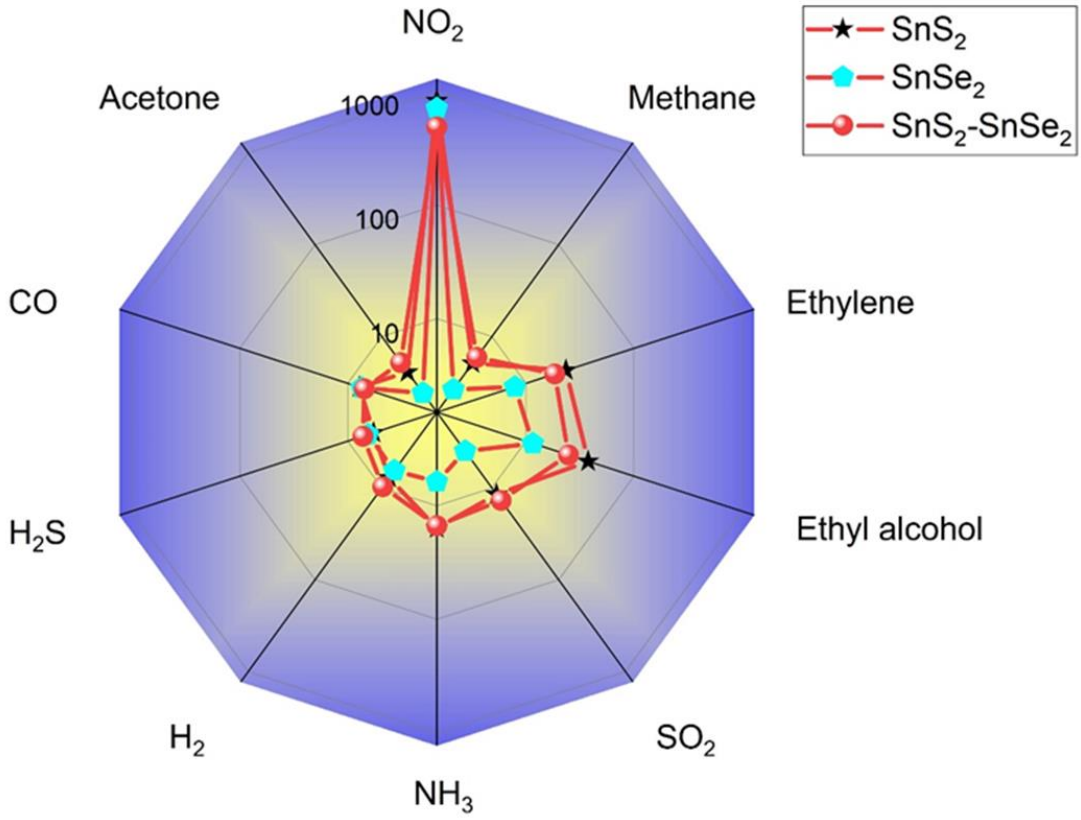

Figure 8: Selectivity plot of the sensors SnS_2 (150°C), SnS_2-$SnSe_2$ (RT), and $SnSe_2$ (RT) demonstrating high selectivity towards NO_2 gas.

References

(1) De Trizio, L.; Manna, L. Forging Colloidal Nanostructures via Cation Exchange Reactions. *Chem. Rev.* **2016**, *116* (18), 10852–10887. https://doi.org/10.1021/acs.chemrev.5b00739.

(2) Jeong, S.; Han, J. H.; Jang, J.; Seo, J.; Kim, J.-G.; Cheon, J. Transformative Two-Dimensional Layered Nanocrystals. *J. Am. Chem. Soc.* **2011**, *133* (37), 14500–14503. https://doi.org/10.1021/ja2049594.

(3) Rivest, J. B.; Jain, P. K. Cation Exchange on the Nanoscale: An Emerging Technique for New Material Synthesis, Device Fabrication, and Chemical Sensing. *Chem. Soc. Rev.* **2013**, *42* (1), 89–96. https://doi.org/10.1039/C2CS35241A.

(4) Hong, Y.; Kim, T.; Jo, J.; Kim, B.; Jin, H.; Baik, H.; Lee, K. Highly Crystalline Hollow Toroidal Copper Phosphosulfide via Anion Exchange: A Versatile Cation Exchange Nanoplatform. *ACS Nano* **2020**, *14* (9), 11205–11214. https://doi.org/10.1021/acsnano.0c02891.

(5) Son, D. H.; Hughes, S. M.; Yin, Y.; Paul Alivisatos, A. Cation Exchange Reactions in Ionic Nanocrystals. *Science (80-.).* **2004**, *306* (5698), 1009–1012. https://doi.org/10.1126/science.1103755.

(6) Lim, Y.; Han, J. H.; Cheon, J. Chemical Transformations of Anisotropic Platelets and Spherical Nanocrystals. *Acc. Chem. Res.* **2021**, *54* (7), 1565–1574. https://doi.org/10.1021/acs.accounts.0c00802.

(7) Goyal, N.; Ram, R.; Rai, R. K.; Ravishankar, N. Electron Microscopy Investigation of Cation Exchange Reaction to Synthesize Lateral Hybrid Nanostructures. *Microsc. Microanal.* **2022**, *28* (S1), 2404–2406. https://doi.org/10.1017/S1431927622009217.

(8) Saruyama, M.; Sato, R.; Teranishi, T. Transformations of Ionic Nanocrystals via Full and Partial Ion Exchange Reactions. *Acc. Chem. Res.* **2021**, *54* (4), 765–775. https://doi.org/10.1021/acs.accounts.0c00701.

(9) Beberwyck, B. J.; Surendranath, Y.; Alivisatos, A. P. Cation Exchange: A Versatile Tool for Nanomaterials Synthesis. *J. Phys. Chem. C* **2013**, *117* (39), 19759–19770. https://doi.org/10.1021/JP405989Z.

(10) Li, X.; Ji, M.; Li, H.; Wang, H.; Xu, M.; Rong, H.; Wei, J.; Liu, J.; Liu, J.; Chen, W.;

Zhu, C.; Wang, J.; Zhang, J. Cation/Anion Exchange Reactions toward the Syntheses of Upgraded Nanostructures: Principles and Applications. *Matter* **2020**, *2*, 554–586. https://doi.org/10.1016/j.matt.2019.12.024.

(11) Huang, X.; Yin, Z.; Wu, S.; Qi, X.; He, Q.; Zhang, Q.; Yan, Q.; Boey, F.; Zhang, H. Graphene-Based Materials: Synthesis, Characterization, Properties, and Applications. *Small* **2011**, *7*, 1876–1902. https://doi.org/10.1002/smll.201002009.

(12) Novoselov, K. S.; Mishchenko, A.; Carvalho, A.; Castro Neto, A. H. 2D Materials and van Der Waals Heterostructures. *Science (80-.).* **2016**, *353* (6298), aac9439. https://doi.org/10.1126/science.aac9439.

(13) Zhang, Y.; Yao, Y.; Sendeku, M. G.; Yin, L.; Zhan, X.; Wang, F.; Wang, Z.; He, J. Recent Progress in CVD Growth of 2D Transition Metal Dichalcogenides and Related Heterostructures. *Adv. Mater.* **2019**, *31* (41), 1901694. https://doi.org/https://doi.org/10.1002/adma.201901694.

(14) Wang, T.; Tan, X.; Wei, Y.; Jin, H. Unveiling the Layer-Dependent Electronic Properties in Transition-Metal Dichalcogenide Heterostructures Assisted by Machine Learning. *Nanoscale* **2022**, *14* (6), 2511–2520. https://doi.org/10.1039/D1NR07747C.

(15) Villaos, R. A. B.; Crisostomo, C. P.; Huang, Z.-Q.; Huang, S.-M.; Padama, A. A. B.; Albao, M. A.; Lin, H.; Chuang, F.-C. Thickness Dependent Electronic Properties of Pt Dichalcogenides. *npj 2D Mater. Appl.* **2019**, *3* (1), 2. https://doi.org/10.1038/s41699-018-0085-z.

(16) Wang, Q. H.; Kalantar-Zadeh, K.; Kis, A.; Coleman, J. N.; Strano, M. S. Electronics and Optoelectronics of Two-Dimensional Transition Metal Dichalcogenides. *Nat. Nanotechnol.* **2012**, *7* (11), 699–712. https://doi.org/10.1038/nnano.2012.193.

(17) Pham, P. V; Bodepudi, S. C.; Shehzad, K.; Liu, Y.; Xu, Y.; Yu, B.; Duan, X. 2D Heterostructures for Ubiquitous Electronics and Optoelectronics: Principles, Opportunities, and Challenges. *Chem. Rev.* **2022**, *122* (6), 6514–6613. https://doi.org/10.1021/acs.chemrev.1c00735.

(18) Geim, A. K.; Grigorieva, I. V. Van Der Waals Heterostructures. *Nature* **2013**, *499* (7459), 419–425. https://doi.org/10.1038/nature12385.

(19) Yu, W. J.; Liu, Y.; Zhou, H.; Yin, A.; Li, Z.; Huang, Y.; Duan, X. Highly Efficient Gate-

Tunable Photocurrent Generation in Vertical Heterostructures of Layered Materials. *Nat. Nanotechnol.* **2013**, *8* (12), 952–958. https://doi.org/10.1038/nnano.2013.219.

(20) Rai, R. K.; Islam, S.; Roy, A.; Agrawal, G.; Singh, A. K.; Ghosh, A.; N., R. Morphology Controlled Synthesis of Low Bandgap $SnSe_2$ with High Photodetectivity. *Nanoscale* **2019**, *11* (3), 870–877. https://doi.org/10.1039/C8NR08138G.

(21) Zheng, B.; Ma, C.; Li, D.; Lan, J.; Zhang, Z.; Sun, X.; Zheng, W.; Yang, T.; Zhu, C.; Ouyang, G.; Xu, G.; Zhu, X.; Wang, X.; Pan, A. Band Alignment Engineering in Two-Dimensional Lateral Heterostructures. *J. Am. Chem. Soc.* **2018**, *140* (36), 11193–11197. https://doi.org/10.1021/jacs.8b07401.

(22) Chen, K.; Wan, X.; Wen, J.; Xie, W.; Kang, Z.; Zeng, X.; Chen, H.; Xu, J.-B. Electronic Properties of MoS_2–WS_2 Heterostructures Synthesized with Two-Step Lateral Epitaxial Strategy. *ACS Nano* **2015**, *9* (10), 9868–9876. https://doi.org/10.1021/acsnano.5b03188.

(23) An, J.; Zhao, X.; Zhang, Y.; Liu, M.; Yuan, J.; Sun, X.; Zhang, Z.; Wang, B.; Li, S.; Li, D. Perspectives of 2D Materials for Optoelectronic Integration. *Adv. Funct. Mater.* **2022**, *32* (14), 2110119. https://doi.org/https://doi.org/10.1002/adfm.202110119.

(24) Schleicher, M.; Fyta, M. Lateral MoS_2 Heterostructure for Sensing Small Gas Molecules. *ACS Appl. Electron. Mater.* **2020**, *2* (1), 74–83. https://doi.org/10.1021/acsaelm.9b00495.

(25) Zhang, Z.; Liu, P.; Song, Y.; Hou, Y.; Xu, B.; Liao, T.; Zhang, H.; Guo, J.; Sun, Z. Heterostructure Engineering of 2D Superlattice Materials for Electrocatalysis. *Adv. Sci.* **2022**, *9* (35), 2204297. https://doi.org/https://doi.org/10.1002/advs.202204297.

(26) Chen, H.; Chen, Z.; Ge, B.; Chi, Z.; Chen, H.; Wu, H.; Cao, C.; Duan, X. General Strategy for Two-Dimensional Transition Metal Dichalcogenides by Ion Exchange. *Chem. Mater.* **2017**, *29* (23). https://doi.org/10.1021/acs.chemmater.7b03523.

(27) Rosati, R.; Paradisanos, I.; Huang, L.; Gan, Z.; George, A.; Watanabe, K.; Taniguchi, T.; Lombez, L.; Renucci, P.; Turchanin, A.; Urbaszek, B.; Malic, E. Interface Engineering of Charge-Transfer Excitons in 2D Lateral Heterostructures. *Nat. Commun.* **2023**, *14* (1), 2438. https://doi.org/10.1038/s41467-023-37889-9.

(28) Goyal, N.; Jagadish, K.; Ravishankar, N. Defect-Mediated Growth of Layered Lateral Bi_2Te_3–Sb_2Te_3–Bi_2Te_3 Heterostructures. *J. Phys. Chem. C* **2024**, *128* (18), 7784–7794.

https://doi.org/10.1021/acs.jpcc.4c01472.

(29) Rai, R. K.; Sarkar, B.; Ram, R.; Nanda, K. K.; Ravishankar, N. Designed Synthesis of a Hierarchical $MoSe_2$@WSe_2 Hybrid Nanostructure as a Bifunctional Electrocatalyst for Total Water-Splitting. *Sustain. Energy Fuels* **2022**, *6* (7), 1708–1718. https://doi.org/10.1039/D1SE01843D.

(30) Gonzalez, J. M.; Oleynik, I. I. Layer-Dependent Properties of SnS_2 and $SnSe_2$ Two-Dimensional Materials. *Phys. Rev. B* **2016**, *94* (12), 125443. https://doi.org/10.1103/PhysRevB.94.125443.

(31) Lu, Z.; Neupane, G. P.; Jia, G.; Zhao, H.; Qi, D.; Du, Y.; Lu, Y.; Yin, Z. 2D Materials Based on Main Group Element Compounds: Phases, Synthesis, Characterization, and Applications. *Adv. Funct. Mater.* **2020**, *30* (40), 2001127. https://doi.org/https://doi.org/10.1002/adfm.202001127.

(32) Camargo Moreira, Ó. L.; Cheng, W.-Y.; Fuh, H.-R.; Chien, W.-C.; Yan, W.; Fei, H.; Xu, H.; Zhang, D.; Chen, Y.; Zhao, Y.; Lv, Y.; Wu, G.; Lv, C.; Arora, S. K.; Ó Coileáin, C.; Heng, C.; Chang, C.-R.; Wu, H.-C. High Selectivity Gas Sensing and Charge Transfer of $SnSe_2$. *ACS Sensors* **2019**, *4* (9), 2546–2552. https://doi.org/10.1021/acssensors.9b01461.

(33) Wu, J.; Wu, Z.; Ding, H.; Wei, Y.; Huang, W.; Yang, X.; Li, Z.; Qiu, L.; Wang, X. Flexible, 3D SnS_2/Reduced Graphene Oxide Heterostructured NO_2 Sensor. *Sensors Actuators B Chem.* **2020**, *305*, 127445. https://doi.org/https://doi.org/10.1016/j.snb.2019.127445.

(34) Wu, R.; Yan, K.; Zhao, J.; Cai, Z.; Jian, S.; Qiu, L. 2D/2D SnS_2/$SnSe_2$ van Der Waals Heterostructure for Highly Sensitive Room-Temperature NO_2 Sensor: Key Role of Interface Contact. *Chem. Eng. J.* **2023**, *466*, 143369. https://doi.org/https://doi.org/10.1016/j.cej.2023.143369.

(35) Han, H.; Yao, Y.; Robinson, R. D. Interplay between Chemical Transformations and Atomic Structure in Nanocrystals and Nanoclusters. *Acc. Chem. Res.* **2021**, *54* (3), 509–519. https://doi.org/10.1021/acs.accounts.0c00704.

(36) Park, J.; Zheng, H.; Jun, Y.; Alivisatos, A. P. Hetero-Epitaxial Anion Exchange Yields Single-Crystalline Hollow Nanoparticles. *J. Am. Chem. Soc.* **2009**, *131* (39), 13943–

13945. https://doi.org/10.1021/ja905732q.

(37) Ha, D.-H.; Moreau, L. M.; Bealing, C. R.; Zhang, H.; Hennig, R. G.; Robinson, R. D. The Structural Evolution and Diffusion during the Chemical Transformation from Cobalt to Cobalt Phosphide Nanoparticles. *J. Mater. Chem.* **2011**, *21* (31), 11498–11510. https://doi.org/10.1039/C1JM10337G.

(38) Shannon, R. D. Revised Effective Ionic Radii and Systematic Studies of Interatomic Distances in Halides and Chalcogenides. *Acta Crystallogr. Sect. A* **1976**, *32* (5), 751–767. https://doi.org/10.1107/S0567739476001551.

(39) Chen, J.; Jiang, F.; Yin, Y. Manipulation of Interfacial Diffusion for Controlling Nanoscale Transformation. *Acc. Chem. Res.* **2021**, *54* (5), 1168–1177. https://doi.org/10.1021/acs.accounts.0c00743.

(40) Ravishankar, N. Seeing Is Believing: Electron Microscopy for Investigating Nanostructures. *J. Phys. Chem. Lett.* **2010**, *1* (8), 1212–1220. https://doi.org/10.1021/jz100163x.

(41) Ou, J. Z.; Ge, W.; Carey, B.; Daeneke, T.; Rotbart, A.; Shan, W.; Wang, Y.; Fu, Z.; Chrimes, A. F.; Wlodarski, W.; Russo, S. P.; Li, Y. X.; Kalantar-zadeh, K. Physisorption-Based Charge Transfer in Two-Dimensional SnS_2 for Selective and Reversible NO_2 Gas Sensing. *ACS Nano* **2015**, *9* (10), 10313–10323. https://doi.org/10.1021/acsnano.5b04343.

(42) Goutham, S.; Sadasivuni, K. K.; Kumar, D. S.; Rao, K. V. Flexible Ultra-Sensitive and Resistive NO_2 Gas Sensor Based on Nanostructured $Zn_{(x)}Fe_{(1-x)2}O_4$. *RSC Adv.* **2018**, *8* (6), 3243–3249. https://doi.org/10.1039/C7RA10478B.

(43) Zhang, D.; Yang, X.; Shen, Y.; Yang, L.; Moreira, Ó. L. C. Manipulation of the $SnSe_2$ Gas Sensing Properties via Au Nanoparticles Decoration. *Surfaces and Interfaces* **2022**, *28*, 101673. https://doi.org/https://doi.org/10.1016/j.surfin.2021.101673.

(44) Liu, W.; Gu, D.; Li, X. AuPt Bimetal-Functionalized $SnSe_2$ Microflower-Based Sensors for Detecting Sub-Ppm NO_2 at Low Temperatures. *ACS Appl. Mater. Interfaces* **2021**, *13* (17), 20336–20348. https://doi.org/10.1021/acsami.1c02500.

(45) Wang, X.; Liu, Y.; Dai, J.; Chen, Q.; Huang, X.; Huang, W. Solution-Processed p-SnSe/n-$SnSe_2$ Hetero-Structure Layers for Ultrasensitive NO_2 Detection. *Chem. – A*

Eur. J. **2020**, *26* (17), 3870–3876. https://doi.org/https://doi.org/10.1002/chem.201905337.

(46) Feng, J.; Chen, J.; Geng, B.; Feng, H.; Li, H.; Yan, D.; Zhuo, R.; Cheng, S.; Wu, Z.; Yan, P. Two-Dimensional Hexagonal SnS_2 Nanoflakes: Fabrication, Characterization, and Growth Mechanism. *Appl. Phys. A* **2011**, *103* (2), 413–419. https://doi.org/10.1007/s00339-010-6032-2.

(47) Sharma, D.; Kumar, R.; Pal, A.; Sakhuja, N.; Bhat, N. Development of a Smart and Ultrafast Flexible Humidity Sensor Using the 0D/2D Au/GeS Heterostructure for Human Respiration Rate Monitoring. *ACS Appl. Electron. Mater.* **2023**, *5* (6), 3162–3171. https://doi.org/10.1021/acsaelm.3c00236.

Table of contents graphic